Range-resolved interferometric signal processing using sinusoidal optical frequency modulation

Thomas Kissinger, Thomas O.H. Charrett and Ralph P. Tatam*

Engineering Photonics, Cranfield University, Cranfield, MK43 0AL, UK

*r.p.tatam@cranfield.ac.uk

Abstract: A novel signal processing technique using sinusoidal optical frequency modulation of an inexpensive continuous-wave laser diode source is proposed that allows highly linear interferometric phase measurements in a simple, self-referencing setup. Here, the use of a smooth window function is key to suppress unwanted signal components in the demodulation process. Signals from several interferometers with unequal optical path differences can be multiplexed, and, in contrast to prior work, the optical path differences are continuously variable, greatly increasing the practicality of the scheme. In this paper, the theory of the technique is presented, an experimental implementation using three multiplexed interferometers is demonstrated, and detailed investigations quantifying issues such as linearity and robustness against instrument drift are performed.

OCIS codes: (060.2370) Fiber optics sensors; (120.2920) Homodyning; (120.3180) Interferometry; (120.5050) Phase measurement.

References and links

1. F. J. Eberhardt and F. A. Andrews, "Laser heterodyne system for measurement and analysis of vibration," J. Acoust. Soc. Am. **48**(3 pt 1), 603–609 (1970).
2. E. Voges, O. Ostwald, B. Schiek, and A. Neyer, "Optical phase and amplitude measurement by single sideband homodyne detection," IEEE J. Quantum Electron. **18**(1), 124–129 (1982).
3. J. Zheng, "Analysis of optical frequency-modulated continuous-wave interference," Appl. Opt. **43**(21), 4189–4198 (2004).
4. D. A. Jackson, A. D. Kersey, M. Corke, and J. D. C. Jones, "Pseudoheterodyne detection scheme for optical interferometers," Electron. Lett. **18**(25), 1081–1083 (1982).
5. R. P. Tatam, J. D. C. Jones, and D. A. Jackson, "Opto-electronic processing schemes for the measurement of circular birefringence," Optica Acta **33**(12), 1519–1528 (1986).
6. A. Dandridge, A. B. Tveten, and T. G. Giallorenzi, "Homodyne demodulation scheme for fiber optic sensors using phase generated carrier," IEEE J. Quantum Electron. **18**(10), 1647–1653 (1982).
7. A. D. Kersey, A. C. Lewin, and D. A. Jackson, "Pseudo-heterodyne detection scheme for the fibre gyroscope," Electron. Lett. **20**(9), 368–370 (1984).
8. I. Sakai, R. Youngquist, and G. Parry, "Multiplexing of optical fiber sensors using a frequency-modulated source and gated output," J. Lightwave Technol. **5**(7), 932–940 (1987).
9. D. A. Shaddock, "Digitally enhanced heterodyne interferometry," Opt. Lett. **32**(22), 3355–3357 (2007).
10. G. A. Cranch and P. J. Nash, "Large-scale multiplexing of interferometric fiber-optic sensors using TDM and DWDM," J. Lightwave Technol. **19**(5), 687–699 (2001).
11. Y. Liao, E. Austin, P. J. Nash, S. A. Kingsley, and D. J. Richardson, "Highly scalable amplified hybrid TDM/DWDM array architecture for interferometric fiber-optic sensor systems," J. Lightwave Technol. **31**(6), 882–888 (2013).
12. G. De Vine, D. S. Rabeling, B. J. Slagmolen, T. T. Lam, S. Chua, D. M. Wuchenich, D. E. McClelland, and D. A. Shaddock "Picometer level displacement metrology with digitally enhanced heterodyne," Opt. Express **17**(2), 828–8377 (2009).

#226258 - $15.00 USD Received 4 Nov 2014; revised 4 Mar 2015; accepted 7 Mar 2015; published 3 Apr 2015

13. A. J. Sutton, O. Gerberding, G. Heinze, and D. A. Shaddock "Digitally enhanced homodyne interferometry," Opt. Express **20**(20), 22195–22207 (2012).
14. T. Kissinger, T. O. H. Charrett, and R. P. Tatam, "Fibre segment interferometry using code-division multiplexed optical signal processing for strain sensing applications," Meas. Sci. Technol. **24**, 094011 (2013).
15. M. Bauer, F. Ritter, and G. Siegmund, "High-precision laser vibrometers based on digital Doppler signal processing," Proc. SPIE **4827**, 50–61 (2002).
16. K. Itoh, "Analysis of the phase unwrapping algorithm," Appl. Opt. **21**(14), 2470–2470 (1982).
17. H. Li, G. B. Rieker, X. Liu, J. B. Jeffries, and R. K. Hanson, "Extension of wavelength-modulation spectroscopy to large modulation depth for diode laser absorption measurements in high-pressure gases," Appl. Opt. **45**(5), 1052–1061 (2006).
18. C. M. Wu and C. S. Su, "Nonlinearity in measurements of length by optical interferometry," Meas. Sci. Technol. **7**(1), 62–68 (1996).
19. T. G. McRae, M. T. L. Hsu, C. H. Freund, D. A. Shaddock, J. Herrmann, and M. B. Gray, "Linearization and minimization of cyclic error with heterodyne laser interferometry," Opt. Lett. **37**(13), 2448–2450 (2012).
20. C. K. Kirkendall, A. D. Kersey, A. Dandridge, M. J. Marrone, and A. R. Davis, "Sensitivity limitations due to aliased high frequency phase noise in high channel-count TDM interferometric arrays," in Optical Fiber Sensors (Optical Society of America, 1996), paper Fr1-4.
21. E. Baumann, F. R. Giorgetta, I. Coddington, L. C. Sinclair, K. Knabe, W. C. Swann, and N. R. Newbury, "Comb-calibrated frequency-modulated continuous-wave ladar for absolute distance measurements," Opt. Lett. **38**(12), 2026–2028 (2013).

1. Introduction

There are many techniques for optical interferometric signal processing, i.e. the extraction of interferometric phase signals from the physically measurable signal by a photo detector. These include heterodyne techniques [1], using a carrier at a fixed frequency typically introduced by a Bragg cell, or schemes such as single-sideband processing [2], where a sawtooth-shaped phase waveform is introduced by a phase modulator. Further techniques, sometimes also referred to as frequency-modulated continuous-wave (FMCW) schemes [3], use optical frequency modulation of the light illuminating an interferometer of non-zero optical path difference (OPD) to induce a carrier signal. This allows self-referencing, passive configurations that offer high stability. Optical frequency modulation can be induced by, for example, laser injection current modulation for diode lasers or diffractive feedback control for external cavity lasers, where common modulation waveforms are of linear (sawtooth or triangular) and sinusoidal shape. Linear techniques, such as pseudo-heterodyne processing [4] are conceptually simple but suffer from the difficulty of cleanly reproducing the modulation waveform due to its high harmonic content [5], while sinusoidal modulation waveforms only contain a single frequency component and are thus easier to control. Often schemes that employ sinusoidal modulation, such as the phase-generated carrier technique [6], use Bessel function analysis to identify at least two harmonics of the modulation frequency that act as carriers, but these do not, however, allow multiple interferometers to be interrogated using only a single laser source and photo detector.

There is a further class of sinusoidal optical frequency modulation techniques that do not evaluate multiple carriers, but instead employ rectangular gating/windowing [7, 8]. Here, the approach by Sakai *et al.* [8], where gating limits the evaluation period to the nearly linear parts of the sinusoidal modulation waveform, also permits range-resolved interferometric signal processing. This is highly desirable [9] as it allows the influence of spurious reflections to be suppressed, if these occur at different ranges to the intended signals, or permits multiple interferometers at different ranges to be multiplexed. However, this approach [8] requires tuning of the phase carrier amplitude to fit integer multiples of the carrier waveform inside the rectangular window, resulting in a discrete set of permitted OPDs of the constituent interferometers. The technique proposed here builds upon this idea of windowing, however, we show that using non-rectangular, smooth window functions, which can easily be applied using digital signal processing, the restriction of fitting integer carrier multiples within the window period vanishes. Additionally, demodulation is now performed using a time-variant carrier frequency

#226258 - $15.00 USD Received 4 Nov 2014; revised 4 Mar 2015; accepted 7 Mar 2015; published 3 Apr 2015

that approximately matches the expected phase modulation waveform at the given OPD of the desired interferometer. Together, these measures allow continuous and independent variation of the OPDs, subject to a minimum separation, of one or more interferometers. Therefore any restriction to adhere to a discrete OPD grid is removed, greatly increasing flexibility and practicality. Also, when compared to other interferometric multiplexing techniques, such as time-division [10, 11] or code-division [9, 12–14], where spatial resolution is proportional to the processing bandwidth, spatial resolution in this approach is proportional to the optical frequency modulation amplitude, thus becoming a property of the laser source. In this way, as will be shown, many GHz can readily be obtained, effectively decoupling spatial resolution from processing bandwidth. In this paper, the theory of technique is explained, before detailing an experimental implementation in a nested Mach-Zehnder interferometric configuration, used to investigate the achievable phase resolution, linearity and tolerance against instrumental drift.

As a general interferometric signal processing technique, the approach described here yields interferometric phase signals that, after appropriate phase unwrapping [16], can be used in a multitude of applications. This includes free-space measurements such as displacement [12, 18, 19] and vibration [15] sensing, as well as fiber-based measurements, such as strain [10, 11, 14] or birefringence [5] sensing. Here, the exact relation between the measured phase signals and the desired measurands are specific to the application as well as to the particular measurement configuration used, but are well-known within the respective fields.

2. Theory

2.1. Basic equations

Here, the analysis of sinusoidal optical frequency modulation presented by Zheng [3] is extended to describe multiple interferometers and the complete demodulation process of the proposed technique. The optical angular frequency, $\omega(t)$, emitted by a source of optical angular center frequency, ω_0, subject to sinusoidal optical frequency modulation of optical angular frequency modulation amplitude, $\Delta\omega$, at modulation angular frequency, ω_m, is then given by:

$$\omega(t) = \omega_0 + \Delta\omega \sin[\omega_\mathrm{m} t] \tag{1}$$

The frequency modulation given by Eq. (1) is also illustrated in Fig. 1(a). The photo detector signal, $U(t)$, resulting from $n = 1...N$ constituent interferometers, each characterized by an individual OPD with corresponding time-of-flight τ_n, can then be given by:

$$U(t) = RP_\mathrm{avg} + \sum_{n=1}^{N} RP_n V_n \cos\left[A_n \sin[\omega_\mathrm{m}(t - t_\mathrm{sp} - 0.5\tau_n)] + \varphi_n(t)\right] \tag{2}$$

Here R is the responsivity of the detector, P_avg is the average power reaching the detector without any interference taking place and t_sp is the signal processing delay. Without loss of generality, t_sp can be set to include all analogue and digital delays occurring from modulation through to processing. For each of the N constituent interferometers present, P_n is the sum of the optical powers of the two arms forming the constituent interferometer, V_n is the mutual interferometric visibility between these two arms and $\varphi_n(t)$ is the desired interferometric phase signal. The phase carrier amplitude, A_n, in units of rads, is the amplitude of the phase modulation waveform that results from the optical frequency modulation at the OPD of the nth interferometer and is given by:

$$A_n = \frac{2\Delta\omega}{\omega_\mathrm{m}} \sin\left[\frac{\omega_\mathrm{m}\tau_n}{2}\right] \quad \approx \quad \Delta\omega\tau_n \text{ for } \tau_n \ll \frac{1}{\omega_\mathrm{m}} \tag{3}$$

Thus, for small τ_n, A_n is independent of the modulation frequency, ω_m, but proportional to the optical angular frequency modulation amplitude of the source, $\Delta\omega$, as well as the time-

#226258 - $15.00 USD Received 4 Nov 2014; revised 4 Mar 2015; accepted 7 Mar 2015; published 3 Apr 2015

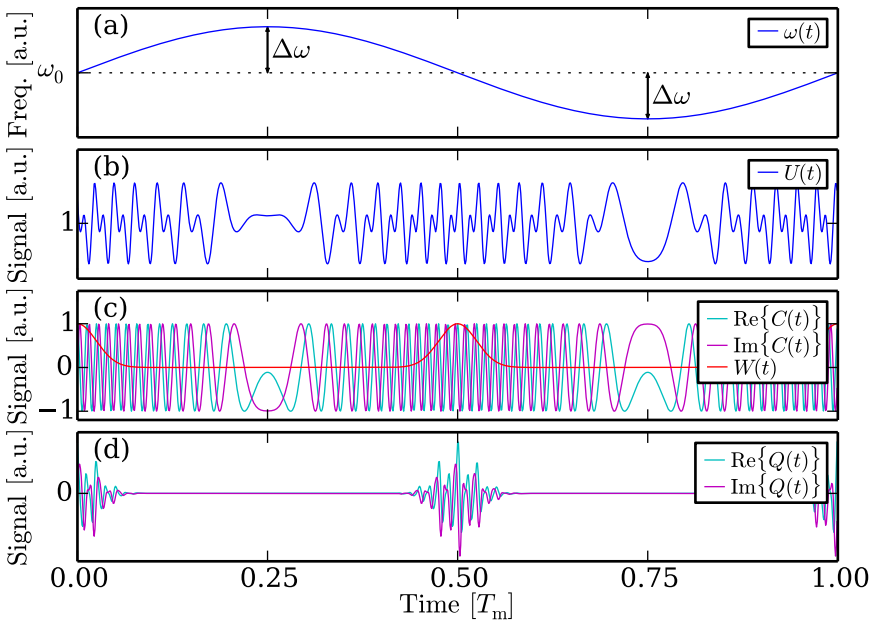

Fig. 1. Illustration of typical signal shapes occurring for the case of two constituent interferometers at $A_1 = 40$ rad and $A_2 = 80$ rad. (a) shows the applied sinusoidal optical frequency modulation, (b) plots the resultant photo detector signal $U(t)$, (c) shows the complex carrier $C(t)$ set for demodulation of the second constituent interferometer by letting $A_\mathrm{d} = A_2$ along with the window function $W(t)$ for width parameter $\sigma = 0.0225$. Finally, (d) plots the resulting complex quadrature signal $Q(t) = W(t)C(t)U(t)$.

of-flight, τ_n, between the arms of the nth interferometer. The latter property permits range-resolved interferometry to be performed with this technique. In general, the usage of the phase carrier amplitude, A_n, instead of OPD or time delay units in the theoretical description allows the analysis of the characteristics of the signal processing, in particular with regard to spatial resolution (detailed in Sec. 2.4 later), independent from the laser source specific parameter $\Delta\omega$.

An example of $U(t)$ for the case of two constituent interferometers at phase carrier amplitudes $A_1 = 40$ rad and $A_2 = 80$ rad, which are typical values for the later experiments, with negligible time-of-flight delays $\tau_1 = \tau_2 \approx 0$, zero-valued signal processing delay $t_\mathrm{sp} = 0$, equal power ratios and equal visibilities, and phases $\varphi_1 = 0$ and $\varphi_2 = 0.5\pi$ is also plotted in Fig. 1(b). After photo detection, the signal $U(t)$ is digitized and separately demodulated for each constituent interferometer. In contrast to regular heterodyne interferometry, where a complex carrier of fixed frequency is used for electronic demodulation [15], the complex carrier, $C(t)$, used in this technique is time-variant and periodic within the modulation period, $T_\mathrm{m} = 2\pi\omega_\mathrm{m}^{-1}$. For each constituent interferometer to be demodulated, $C(t)$ is chosen to approximately match the phase modulation waveform resulting from the applied sinusoidal optical frequency modulation using the demodulation phase carrier amplitude, A_d, and demodulation time-of-flight delay, τ_d, as parameters and $C(t)$ is given by:

$$C(t) = \exp\left[\mathrm{j}A_\mathrm{d}\sin[\omega_\mathrm{m}(t - t_\mathrm{sp} - 0.5\tau_\mathrm{d})]\right] \tag{4}$$

A typical representation of $C(t)$ is also plotted in Fig. 1(c), where for the example configuration described earlier, the second constituent interferometer is selected for demodulation by letting $A_\mathrm{d} = A_2 = 80$ rad and $\tau_\mathrm{d} = \tau_2 \approx 0$. After demodulation with $C(t)$ the resulting complex

#226258 - $15.00 USD Received 4 Nov 2014; revised 4 Mar 2015; accepted 7 Mar 2015; published 3 Apr 2015

quadrature signal, $Q(t)$, is then given by:

$$\begin{aligned} Q(t) &= W(t)C(t)U(t) \\ &= W(t)RP_{\mathrm{avg}}\exp\left[\mathrm{j}A_{\mathrm{d}}\sin[\omega_{\mathrm{m}}(t-t_{\mathrm{sp}}-0.5\tau_{\mathrm{d}})]\right] + W(t)R\sum_{n=1}^{N}0.5P_nV_n\Big\{ \\ &\quad \exp\left[\mathrm{j}\left(A_{\mathrm{d}}\sin[\omega_{\mathrm{m}}(t-t_{\mathrm{sp}}-0.5\tau_{\mathrm{d}})] - A_n\sin[\omega_{\mathrm{m}}(t-t_{\mathrm{sp}}-0.5\tau_n)] - \varphi_n(t)\right)\right] \\ &\quad + \exp\left[\mathrm{j}\left(A_{\mathrm{d}}\sin[\omega_{\mathrm{m}}(t-t_{\mathrm{sp}}+0.5\tau_{\mathrm{d}})] + A_n\sin[\omega_{\mathrm{m}}(t-t_{\mathrm{sp}}-0.5\tau_n)] + \varphi_n(t)\right)\right]\Big\} \end{aligned} \tag{5}$$

Here, $W(t)$ is an additional window function that is periodic in T_{m} and is specified later in Eq. (8). A typical representation of the window function is also plotted in Fig. 1(c) and used to obtain the complex quadrature signal $Q(t)$, shown in Fig. 1(d) for the earlier example case.
In general, to simplify Eq. (5) relevant to the later experiments, both τ_{d} and τ_n can be considered negligible relative to the modulation period, i.e. $|\tau_{\mathrm{d}}| \ll T_{\mathrm{m}}$ and $|\tau_{\mathrm{n}}| \ll T_{\mathrm{m}}$. These assumptions allow rewriting of Eq. (5) using generic complex exponential terms, $E(t,A,\varphi(t))$, given by:

$$E\left(t,A,\varphi(t)\right) = \exp\left[\mathrm{j}\Big(A\sin[\omega_m(t-t_{\mathrm{sp}})] + \varphi(t)\Big)\right] \tag{6}$$

Here A is representative of any combination of $A = A_{\mathrm{d}} + [0, \pm A_n]$ occurring in the simplified version of $Q(t)$ below, where the described assumptions of zero τ_{d} and τ_n were used:

$$\begin{aligned} Q(t) &\approx W(t)RP_{\mathrm{avg}}E\left(t,A_{\mathrm{d}},0\right) + W(t)R\sum_{n=1}^{N}0.5P_nV_n\Big\{ \\ &\quad E\left(t,(A_{\mathrm{d}}-A_n),-\varphi_n(t)\right) + E\left(t,(A_{\mathrm{d}}+A_n),\varphi_n(t)\right)\Big\} \end{aligned} \tag{7}$$

When the demodulation phase carrier amplitude, A_{d}, of the complex carrier, $C(t)$, of Eq. (4) is chosen to match the phase carrier amplitude of the desired nth interferometer, i.e. $A_{\mathrm{d}} = A_n$, the sinusoidal part of the complex exponential term $E(t,(A_{\mathrm{d}}-A_n),-\varphi_n(t))$ in the approximated version of the complex quadrature signal $Q(t)$, given by Eq. (7), vanishes because $A = A_{\mathrm{d}} - A_{\mathrm{n}} = 0$. The desired phase signal, $\varphi_n(t)$, is then directly encoded in the baseband signal component of this term $E(t,(A_{\mathrm{d}}-A_n),-\varphi_n(t)) = \exp[-\mathrm{j}\varphi_n(t)]$. However, the presence of the other complex exponential terms with $A \neq 0$ in Eq. (7) prohibits straightforward phase extraction, because, in general, each of these terms also adds its own baseband signal components to $Q(t)$. If, however, the window function, $W(t)$, is chosen such that the baseband components of all complex exponential terms with sufficiently large phase carrier amplitudes, A, are suppressed in Eq. (7), then only the desired term $E(t,(A_{\mathrm{d}}-A_n),-\varphi_n(t)) = \exp[-\mathrm{j}\varphi_n(t)]$ contributes significantly to the baseband component of $Q(t)$ and undesired crosstalk from the baseband components of other complex exponential terms can be avoided. In this case $\varphi_n(t)$ can be recovered using an arctan function on the low-pass filtered version of $Q(t)$. This is the key working principle of this technique and the baseband crosstalk suppression behavior will be quantified and explained in more detail in the following sections.

In this scheme, for each modulation period of length T_{m}, we use two windows that are centered on the fast-moving sections of the complex exponential terms, as illustrated in Fig. 1(c). The shape of the individual windows is given by a Gaussian function, with a width specified by the width parameter σ, the Gaussian standard deviation. The complete window function, $W(t)$, periodic in T_{m} and incorporating the two individual Gaussian windows is then given by:

$$W(t) = \sum_{n=-\infty}^{\infty}\left\{\exp\left[-\frac{1}{2}\left(\frac{(t-t_{\mathrm{sp}})-nT_{\mathrm{m}}}{T_{\mathrm{m}}\sigma}\right)^2\right] + \exp\left[-\frac{1}{2}\left(\frac{(t-t_{\mathrm{sp}})-(n+0.5)T_{\mathrm{m}}}{T_{\mathrm{m}}\sigma}\right)^2\right]\right\} \tag{8}$$

#226258 - $15.00 USD Received 4 Nov 2014; revised 4 Mar 2015; accepted 7 Mar 2015; published 3 Apr 2015

Here, $W(t)$ is stated for the assumptions of $\tau_d \approx 0$ and $\tau_n \approx 0$. It is stressed that above version of $W(t)$ is only an initial choice and other window functions remain to be explored. It will be shown in Sec. 4.2 by Fig. 11(c) that for our experimental implementation, the best choice of σ is approximately 0.0225, therefore this value is used in the following theoretical analysis. It is, however, emphasized that, as experimentally confirmed by Fig. 11(c), the technique can work over a wide range of the parameter σ with only small performance penalties.

2.2. *Baseband suppression properties for a single complex exponential term*

Before discussing the complete demodulation represented by all terms in Eq. (7), it is instructive to first investigate the effect of the window function, $W(t)$, on the suppression of the baseband component of a single, generic complex exponential term $E\big(t,A,\varphi(t)\big)$ of Eq. (6). This is illustrated in Fig. 2 for an example term $E(t,40,0)$, where $A = 40$ rad is a typical value for the phase carrier amplitude used in the later experiments. Figure 2(a) plots the real and imaginary parts of $E(t,40,0)$ as well as $W(t)$, given by Eq. (8) at $\sigma = 0.0225$, in the time domain, while Fig. 2(b) compares the corresponding Fourier transformed spectra with and without application of $W(t)$. Note that the phase term, $\varphi(t)$, in Eq. (6) has no influence on baseband suppression and can be ignored, as can the signal processing delay, t_{sp}, which is considered digitally compensated and thus zero-valued. It can clearly be seen in Fig. 2(b) that the rejection of the low-frequency

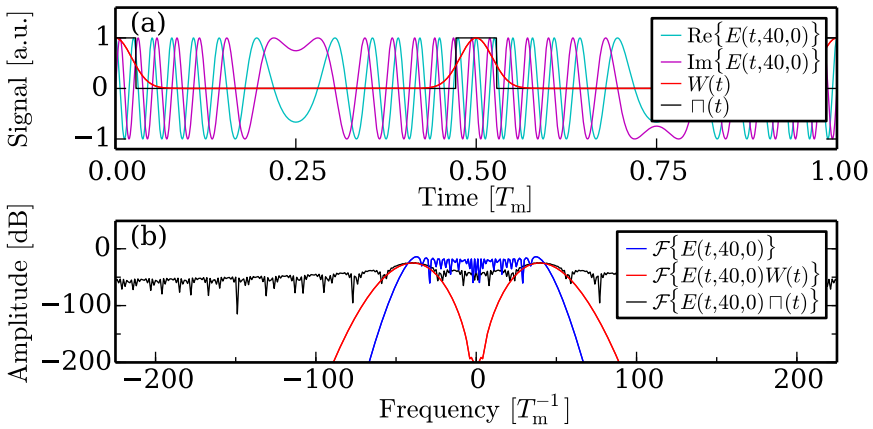

Fig. 2. Illustration of the effect of windowing on the baseband component of a single complex exponential term $E(t,40,0)$. (a) plots the real and imaginary part of $E(t,40,0)$ over one modulation period T_m as well as $W(t)$ for $\sigma = 0.0225$ and, additionally, a rectangular window function $\sqcap(t)$ for comparison with prior work. (b) compares the corresponding amplitude spectra of $E(t,40,0)$ with and without application of $W(t)$ or $\sqcap(t)$.

parts of the phase modulation waveform through the application of the smooth window function $W(t)$ has a very significant effect in reducing the signal amplitude in the baseband. This creates a distinctly peaked signal spectrum with maxima at frequencies $\approx \pm 40\,T_m^{-1} \approx \pm A T_m^{-1}$ and without any side-lobe energy, which contrasts with the spectrum resulting from the application of a rectangular window $\sqcap(t)$ in prior work by Sakai *et al.* [8], also included in Fig. 2(a) and 2(b) for comparison. This lack of side-lobe energy of the complex exponential terms allows the continuously variable placement of the OPDs of the constituent interferometers, which is a key advantage of the proposed technique over prior work. Figure 3 quantifies this behavior by plotting the baseband crosstalk suppression, i.e. the ratio between the undesired signal energy entering the baseband and the total signal energy, versus the phase carrier amplitude, A, of a generic complex exponential term, $E(t,A,0)$, for a range of window width parameters σ.

#226258 - $15.00 USD Received 4 Nov 2014; revised 4 Mar 2015; accepted 7 Mar 2015; published 3 Apr 2015

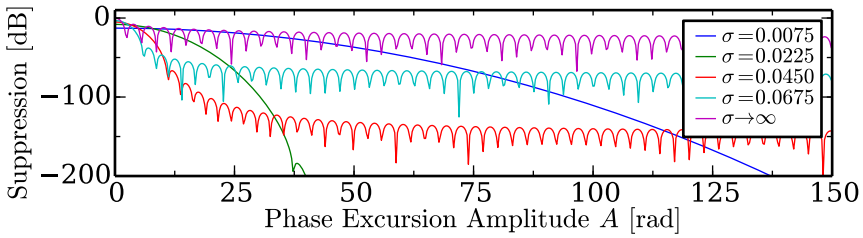

Fig. 3. The baseband crosstalk suppression that results from applying $W(t)$ of Eq. (8) to a complex exponential term of Eq. (6) is plotted as a function of phase carrier amplitude A for a range of window width parameters σ and without windowing, i.e. $\sigma \to \infty$

2.3. *Baseband suppression properties for the complete demodulation process*

The results on baseband suppression on a single generic complex exponential term $E(t,A,\varphi(t))$ described in the previous section can be extended to include every complex exponential term that is present in the approximated version of the complex quadrature signal $Q(t)$ given by Eq. (7). This is possible because all complex exponential terms in Eq. (7) form a linear combination and thus add independently in the Fourier domain. Figure 4 illustrates this behavior in the frequency domain by highlighting the effect of the application of the window function, $W(t)$, on $Q(t)$. Here, the earlier example of $Q(t)$, also depicted in the time domain in Fig. 1(d), resulting from the demodulation of the second of two constituent interferometers at phase carrier amplitudes $A_1 = 40$ rad and $A_2 = 80$ rad, is used. It can be seen in Fig. 4 that without windowing ($\sigma \to \infty$) the spectrum is widely spread out, while for windowing at width parameter $\sigma = 0.0225$ distinct peaks are observable that correspond to the different complex exponential terms of Eq. (7). By analysis of the possible values of the phase carrier amplitudes A of the five complex exponential terms present in Eq. (7) in this case, it can be seen that in the baseband, the spectrum originates solely from the convolution of the term $E(t,(A_\mathrm{d}-A_2),\varphi_2(t)) = \exp[-\mathrm{j}\varphi_2(t)]$ with $W(t)$. Here, the sinusoidal component of the complex exponential term cancels because $A = A_\mathrm{d} - A_2 = 0$ rad. The desired phase signal, $\varphi_2(t)$, can then be recovered from the baseband component of $Q(t)$ without crosstalk from other terms present in Eq. (7).

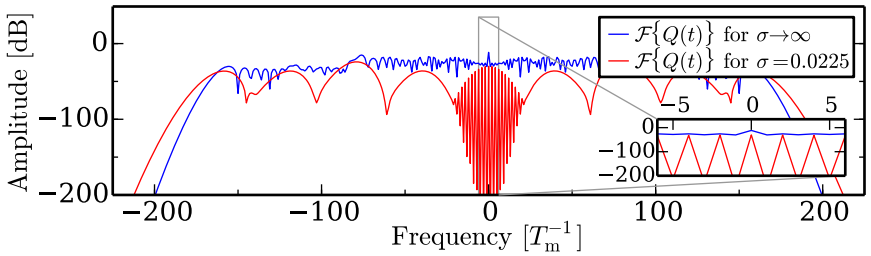

Fig. 4. Illustration of the effect of the application of the window function $W(t)$. Here the complex quadrature signal $Q(t)$ for the example configuration previously used for Fig. 1 is plotted in the frequency domain, comparing the cases with ($\sigma = 0.0225$) and without ($\sigma \to \infty$) windowing. Here, for the case with windowing, the spectrum separates into distinct peak regions and the inset reveals the resulting comb-like spectrum in the baseband.

It can also be seen in Fig. 4 that the convolution of the desired term, $\exp[-\mathrm{j}\varphi_2(t)]$, which is ideally a delta peak centered at zero frequency, with the periodic window function, $W(t)$, leads to a set of carrier harmonics that limit the unambiguous measurement bandwidth. Because $W(t)$ of Eq. (8) is periodic in $2f_\mathrm{m}$, a comb-like structure, visible in the inset in Fig. 4, arises

#226258 - $15.00 USD Received 4 Nov 2014; revised 4 Mar 2015; accepted 7 Mar 2015; published 3 Apr 2015

in the baseband, yielding a theoretical unambiguous measurement bandwidth of f_{m}. However, in practice, weak carrier components at $\pm f_{\mathrm{m}}$ appear due to non-perfect matching of the phase carrier amplitude A_n of the actual interferometer to the value of A_{d} that is used for demodulation, leading to usable unambiguous measurement bandwidth of $0.5 f_{\mathrm{m}}$. To extract the desired phase signal from the complex quadrature signal, $Q(t)$, then requires low-pass filtering of $Q(t)$ at a cut-off frequency $\leq 0.5 f_{\mathrm{m}}$, followed by complex phase determination and finally phase unwrapping [16]. This theoretical treatment neglects any intensity modulation that is normally associated with laser injection current modulation, or any deviation from a purely sinusoidal optical frequency modulation waveform. As will be shown later, these effects may be present in a real experiment but their influence is limited and can be corrected to improve performance.

2.4. Spatial resolution

The suppression of unwanted complex exponential terms through the application of the window function can be quantified by the baseband crosstalk suppression ratio, as plotted in Fig. 3. In order to establish a formula for the minimum OPD separation between constituent interferometers it is necessary to specify an acceptable baseband crosstalk suppression level in the design of the implementation. For a given window width parameter, σ, the corresponding minimum phase carrier amplitude, A_{min}, at the baseband crosstalk suppression level can then be extracted from Fig. 3 and $A > A_{\mathrm{min}}$ has to be exceeded by all complex exponential terms in Eq. (7) apart from the desired baseband term, where $A \approx 0$, in order for the technique to work as specified. The determined value for A_{min} can then be inserted into to the following formula for $\mathrm{OPD}_{\mathrm{min}}$ that is derived from the approximated version of Eq. (3), where c is the speed of light:

$$\mathrm{OPD}_{\mathrm{min}} \approx c \frac{A_{\mathrm{min}}}{\Delta\omega} \tag{9}$$

In this technique, $\mathrm{OPD}_{\mathrm{min}}$ is the minimum OPD that has to be maintained for a single interferometer, or, for multiple constituent interferometers, the minimum OPD of the first interferometer and the minimum OPD separation between any subsequent constituent interferometers. This highlights that in this technique spatial resolution is dependent on a subjective choice of an acceptable baseband crosstalk suppression level. As an example, at a window width of $\sigma = 0.0225$ and for a chosen baseband crosstalk suppression level of $-200\,\mathrm{dB}$, Fig. 3 yields a value $A_{\mathrm{min}} = 40\,\mathrm{rad}$. For an optical frequency modulation amplitude of $\Delta\omega(2\pi)^{-1} = \Delta f = 9\,\mathrm{GHz}$, the value used in the practical implementation described later, Eq. (9) yields $\mathrm{OPD}_{\mathrm{min}} = 0.21\,\mathrm{m}$, which is equivalent to a physical path difference of $0.15\,\mathrm{m}$ in a typical optical fiber with group index of refraction $n = 1.46$.

3. Experiment

3.1. Setup and processing

A suitable setup to test the proposed signal processing technique is the nested Mach-Zehnder (MZ) interferometric configuration shown in Fig. 5, which is constructed using regular SMF28e+ fiber and where test signals can be introduced using Piezo-electric fiber stretchers (PZT). The nested MZ configuration includes an inner interferometer, consisting of arms A and B, subsequently referred to as interferometer 1 (I1), while the extra outer arm C gives rise to two additional interferometers, referred to as interferometer 2 (I2) for the interference of arms B&C and interferometer 3 (I3) for the interference of arms A&C. Test signals can be introduced by PZT A into arm A and PZT C into arm C. The physical path lengths were designed to increase by at least $0.15\,\mathrm{m}$ per constituent interferometer, corresponding to the spatial resolution calculated in Sec. 2.4. When measured with a Luna OBR 4400 Reflectometer the actual physical path differences were found to be $0.15\,\mathrm{m}$, $0.35\,\mathrm{m}$ and $0.50\,\mathrm{m}$ for I1, I2 and I3, respectively. The

#226258 - $15.00 USD Received 4 Nov 2014; revised 4 Mar 2015; accepted 7 Mar 2015; published 3 Apr 2015

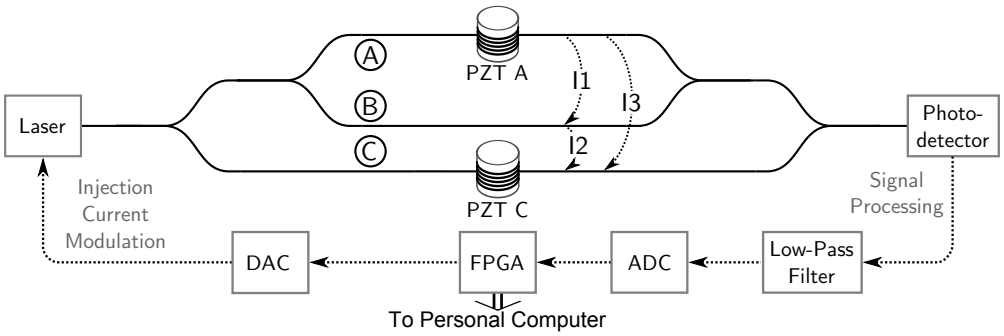

Fig. 5. The experimental setup used in this paper is a nested MZ interferometer with arms A, B and C, where the three constituent interferometers I1, I2 and I3 correspond to the interference between arms A&B, B&C and A&C, respectively. PZTs are integrated in arms A and C to induce suitable test signals. Both modulation and signal processing are controlled by an Field Programmable Gate Array (FPGA) via digital-to-analogue (DAC) and analogue-to-digital (ADC) converters, respectively. The FPGA performs time-critical demodulation steps and sends the data to a personal computer for final processing.

nested MZ setup was chosen because of the novel measurement possibilities range-resolved interferometry can offer, here allowing the differential signal induced by PZT A as well as the common-mode offset signal induced by PZT C to be measured simultaneously with a single continuous-wave laser and photo detector. It is also important to note that both the differential and the offset signal can be derived in two ways, either measured directly by the signals from I1 or I2, respectively, or by subtracting the signals of the other two constituent interferometers, allowing a straightforward way to assess the performance of the technique.

In the experimental setup shown in Fig. 5, the laser diode (Eblana Photonics EP1550-NLW-B; center wavelength: 1551 nm, power: 6 mW at $I_{\mathrm{bias}} = 125$ mA; line width: 1 MHz using Profile LDC200 driver) was modulated by a sinusoidal injection current waveform with a peak-to-peak amplitude of 90 mA at a modulation frequency of $f_{\mathrm{m}} = 98$ kHz, resulting in an optical frequency modulation of amplitude $\Delta\omega(2\pi)^{-1} = \Delta f = 9$ GHz as measured with an optical spectrum analyzer. All modulation and signal processing functions are controlled by a Field Programmable Gate Array (FPGA) to ensure precisely synchronized modulation and demodulation. The FPGA (Altera Cyclone IV on Terasic DE2-115 board) is connected to a data acquisition daughter board that runs at a sample rate of 150 MHz at 14 bits resolution. Here, the digital-to-analogue converter (DAC) is used to create the sinusoidal modulation signal for the laser diode and the analogue-to-digital converter (ADC) samples the data from the photo detector, which has been low-pass anti-aliasing filtered with a cut-off at 50 MHz. In the current implementation eight range channels can be demodulated simultaneously by the FPGA, and, for each channel, the resultant complex quadrature signal, $Q(t)$, is low-pass filtered down to an unambiguous measurement bandwidth of $0.5 f_{\mathrm{m}} = 48$ kHz before being sent to a personal computer (PC). The PC initially programs the look-up tables used to preform the demodulation in the FPGA and then continuously performs complex phase evaluation and unwrapping for each range channel, although this could, in principle, also be performed in the FPGA in future implementations.

3.2. Signal and modulation properties

Figure 6(a) shows a typical photo detector signal, $U(t)$, over one modulation period, T_{m}, arising from the three constituent interferometers present in the setup of Fig. 5. When the symmetry center of $U(t)$ in Fig. 6(a) is compared to Fig. 1(b), a signal processing delay, t_{sp}, of approx-

#226258 - $15.00 USD Received 4 Nov 2014; revised 4 Mar 2015; accepted 7 Mar 2015; published 3 Apr 2015

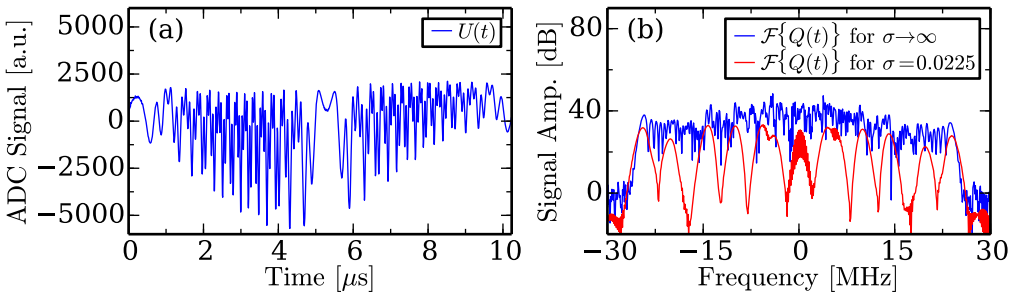

Fig. 6. (a) plots the photo detector signal $U(t)$, sampled by the ADC, over one modulation period. Analogous to Fig. 4, (b) shows the Fourier spectrum after demodulating at $A_\mathrm{d} = 103$ rad with ($\sigma = 0.0225$) and without ($\sigma \to \infty$) application of the window function $W(t)$. Here the signal processing delay t_sp has been compensated as described later in Sec. 3.3.

imately a quarter of T_m can be observed. Figure 6(b) illustrates the demodulation in the frequency domain at a demodulation phase carrier amplitude $A_\mathrm{d} = 103$ rad, corresponding to the approximate value of A_2 expected for interferometer 2 (I2). Analogous to Fig. 4, the effect of the separation of the spectra of the complex exponential terms into distinct peak regions can be seen in Fig. 6(b) when the window function $W(t)$ of Eq. (8) with $\sigma = 0.0225$ is applied.

In Fig. 6(a), a strong intensity modulation envelope of the photo detector signal $U(t)$ is visible. In order to determine the parameters of this intensity modulation for later correction, analysis was performed using an oscilloscope to display the output signal of a photo detector connected to a separate, single MZ interferometer with a large OPD imbalance of ≈ 25 m. In this case, when optical frequency modulation is applied, the bulk of the interference fringes change so fast that they are low-pass filtered by the detector bandwidth of 80 MHz, allowing the measurement of the sinusoidal intensity modulation amplitude and delay. Additionally, slow fringes near the frequency modulation zero-crossings, as seen in Figs. 1(a) and 1(b), remain visible and the determination of their symmetry center allows the frequency-modulation to intensity-modulation phase shift, δ, to be measured, which is generally present in laser diodes undergoing rapid injection current modulation [17]. For our laser, the intensity modulation depth, D, i.e. the ratio between the intensity modulation amplitude and average intensity, was found to be $D = 0.45$, while the phase shift, δ, was measured at 208°, which is comparable to literature [17]. In addition to intensity modulation, a deviation of the optical frequency modulation waveform from its ideal sinusoidal shape due to the slightly non-linear injection current tuning characteristic of a laser diode is also expected. Here, this deviation was determined by interferometric phase measurement of the phase signals resulting from the described injection current modulation within a single MZ interferometer of 4 cm physical path difference, using an electro-optic phase modulator and high-speed single-sideband signal processing technique [2, 14]. In this way, the harmonics were found to be 4.1% of the main sinusoidal frequency amplitude at 12° phase shift for the first harmonic and 0.3% at 120° phase shift for the second harmonic, where, due to their small value, the second and all higher harmonics have been subsequently neglected.

To correct the influences of intensity modulation, it is sufficient to simply divide the raw photo detector signal $U(t)$ by the previously determined intensity modulation profile. To correct the non-linear deviations of the sinusoidal optical frequency modulation waveform, the complex carrier signal, $C(t)$ of Eq. (4), can be extended by a first harmonic sinusoidal term in the exponential at double the modulation frequency using the determined relative strength and phase shift values. Both types of corrections can straightforwardly be incorporated into

#226258 - $15.00 USD Received 4 Nov 2014; revised 4 Mar 2015; accepted 7 Mar 2015; published 3 Apr 2015

the FPGA look-up tables used for demodulation. However, one of the aims of this paper is to show the robustness of the proposed technique and prove that high-quality measurements can be made even without performing these corrections. Therefore, throughout the remainder of this paper there will be a comparison between so-called corrected and uncorrected results.

3.3. *Determination of demodulation parameters*

For the practical operation of the proposed technique, the correct demodulation parameters, i.e. the signal processing delay, t_{sp}, as well as the approximate phase modulation amplitudes, A_n, for each constituent interferometer have to be identified without any prior knowledge, where the time-of-flight delays τ_n can be neglected under the assumptions that lead to Eq. (7). Both t_{sp} and the values for A_n can be found by plotting a map of baseband signal amplitude of the low-pass filtered complex quadrature signal $Q(t)$ as a function of the demodulation parameters A_d and t_{sp}. These maps are shown in Fig. 7(a) without and in Fig. 7(b) with the corrections that were previously discussed in Sec. 3.2, where a window width parameter of $\sigma = 0.0225$ was used throughout. It is stressed that these maps stem from experimental data and that they have been calculated over only a single modulation period, using the same data set also plotted in Fig. 6(a). The resulting maps have patterns that consist of a set of nodes spread horizontally for each of the three constituent interferometers present. The horizontal distance between the nodes decreases proportionally with the phase carrier amplitude A_n of the nth constituent interferometer. The horizontal patterning seen in the maps can only be explained using the unapproximated equations for the complex quadrature signal $Q(t)$ that are given by Eq. (5). However, in both maps a set of nodes that overlap vertically can be found and a line, shown in white on the maps, can be drawn connecting the centers of these nodes. This line marks the correct signal processing delay, t_{sp}, and the assumptions used to obtain the approximated version of $Q(t)$ given by Eq. (7) are valid here. In this work, all signal processing was carried out on this line by digitally compensating t_{sp} in the demodulation look-up tables, where $t_{sp} = 2775$ ns was found from both Figs. 7(a) and 7(b). The peak positions in the graphs on the right of Figs. 7(a) and 7(b), which plot the information along the white evaluation line in a logarithmic scale, can then be used to extract the phase carrier amplitudes. Here, values of $A_1 = 43.5$ rad, $A_2 = 103.0$ rad and $A_3 = 146.5$ rad were found and subsequently used to demodulate the signals of I1, I2 and I3.

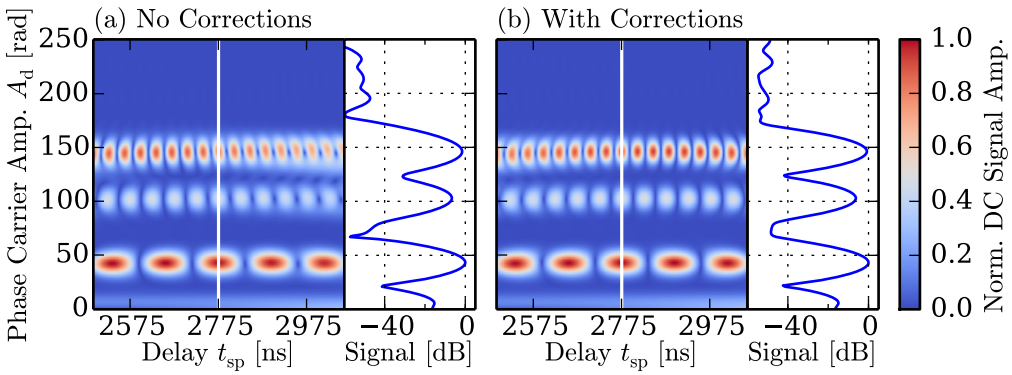

Fig. 7. Determination of demodulation parameters using demodulation phase carrier amplitude A_d versus signal processing delay t_{sp} maps with $\sigma = 0.0225$ for the cases without corrections (a) and with corrections (b) according to Sec. 3.2. The maps plot the normalized baseband signal amplitude as a function of A_d and t_{sp} with a common colorbar shown on the right. The white, vertical line is the chosen evaluation location and the signal along this line is also plotted next to each map on a logarithmic scale.

#226258 - $15.00 USD Received 4 Nov 2014; revised 4 Mar 2015; accepted 7 Mar 2015; published 3 Apr 2015

4. Results and discussion

4.1. Phase measurements

Using the operating conditions and demodulation parameters described in Sec. 3, measurements employing the nested MZ interferometer shown in Fig. 5 with sinusoidal test signals of frequency 10 Hz at peak-to-peak phase amplitude 7.2 rad, induced by PZT A, and of frequency 180 Hz at peak-to-peak phase amplitude 6.8 rad, induced by PZT C, were performed. For these excitations, a typical time trace of a low-pass filtered, complex quadrature signal can be seen in Fig. 8(a) for interferometer I1. Figure 8(b) shows the corresponding polar plots for the quadrature signals for I1, I2 and I3, recording the complex values of every data point over a period of 5 s. On visual inspection the polar plots are found to be both concentric and highly circular, where both concentricity and circular shape are requirements for linear measurements in the absence of cyclic errors [18]. In the measurement data shown in Figs. 8(a) and 8(b) none of the corrections discussed in Sec. 3.2 have been applied, while the corresponding graphs using these corrections appear virtually identical. In Fig. 8(b) the three signals differ in their complex amplitude in the same ratio that is also observable from the signal amplitudes on the right-hand side of Fig. 7(a).

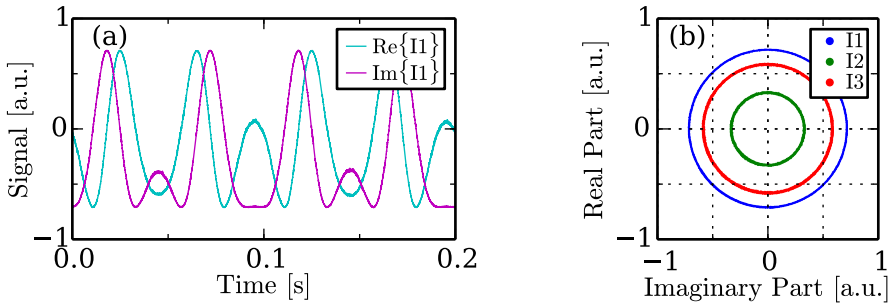

Fig. 8. The low-pass filtered, complex quadrature signal $Q(t)$ is shown in (a) as a time series over 0.2 s for I1 without any corrections discussed previously in Sec. 3.2, while (b) shows the polar plots of all three constituent interferometers in the complex plane.

Figure 9 then shows the time traces of the unwrapped phase signals from the experiment described above, also without any corrections according to Sec. 3.2 applied. Figure 9(a) plots the signals from the three constituent interferometers over 0.2 s, while the inset shows the same signals over an extended time period of 5 s. As discussed previously, the nested MZ interferometer configuration of Fig. 5 permits the common-mode offset signal, induced by PZT C, to be recovered in two ways, directly from I2 or indirectly by subtracting the signals from I3 and I1. Both these signals are compared in Fig. 9(b), again with an additional inset over 5 s, along with their difference signal, referred to as residual signal in the following. Analogously, the differential signal, induced by PZT A, can be recovered in a direct version from I1 or indirectly by subtracting the signals from I3 and I2, which is shown in Fig. 9(c) along with their residual difference signal. It is found that both residual signals of Figs. 9(b) and 9(c) are given by the same equation (I3 - I2 - I1) and are thus mathematically and numerically equal, with Fig. 9(d) plotting the residual signal in detail. A low-pass filtered version of the residual signal at a cut-off frequency of 600 Hz is also shown in Fig. 9(d). The inset in Fig. 9(d) shows that the filtered residual signal stays remarkably constant, highlighting the high quality of the measurements that can be achieved with the presented technique. Nevertheless, the residual signal should theoretically be zero-valued, even in the presence of laser wavelength drift or laser frequency noise, because the OPDs of the direct and indirect signals mathematically cancel, whilst in Fig. 9(d) it can be

#226258 - $15.00 USD Received 4 Nov 2014; revised 4 Mar 2015; accepted 7 Mar 2015; published 3 Apr 2015

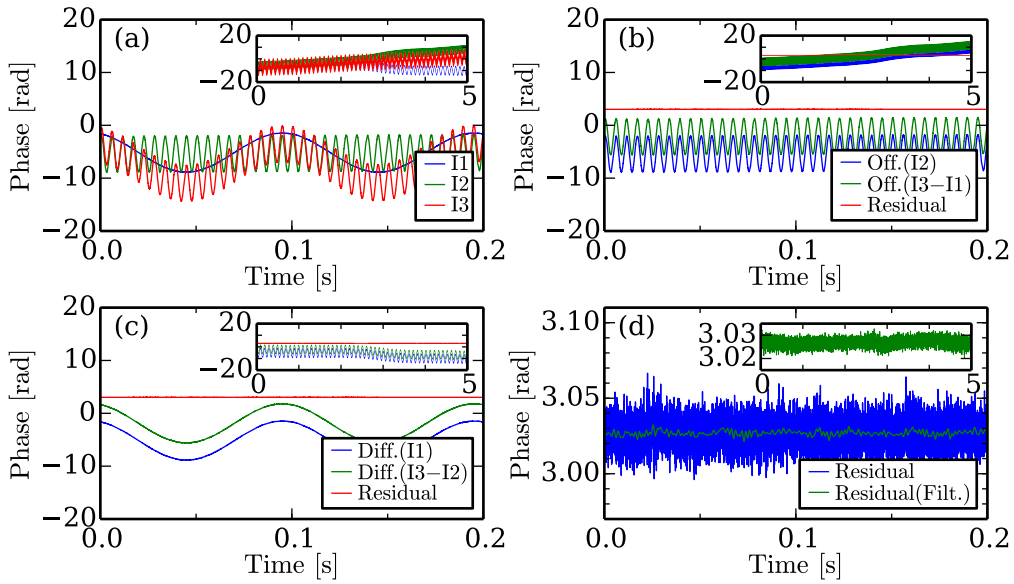

Fig. 9. Time traces of the phase signals over 0.2 s in the main plots and over 5 s in the insets are shown without any corrections according to Sec. 3.2. (a) plots the signals from the three constituent interferometers I1, I2 and I3, exhibiting excitations at 10 Hz from PZT A (in I1 and I3) and at 180 Hz from PZT C (in I2 and I3). (b) plots the offset signals (induced by PZT C) obtained directly (I2) or indirectly (I3 - I1) along with their difference, the residual signal. (c) shows the differential signal (induced by PZT A) obtained directly (I1) or indirectly (I3 - I2), again with the residual signal as their difference. (d) plots only the residual signal (I3 - I2 - I1), mathematically identical for both (b) and (c). Here a low-pass filtered signal (cut-off at 600 Hz) is also plotted and the inset only shows the filtered signal.

seen to have a mean value of 3.03 rad, with additional measurements not shown here indicating that long-term changes of the residual signal phase can also occur. It is thought that this is a manifestation of the, in general, unrelated polarization states of the light within the fiber arms, leading to OPD values of the constituent interferometers that are minutely different from those expected when polarization dependence is neglected. This could explain the observed non-zero phase values in the residual signal as well as any associated slow drifts.

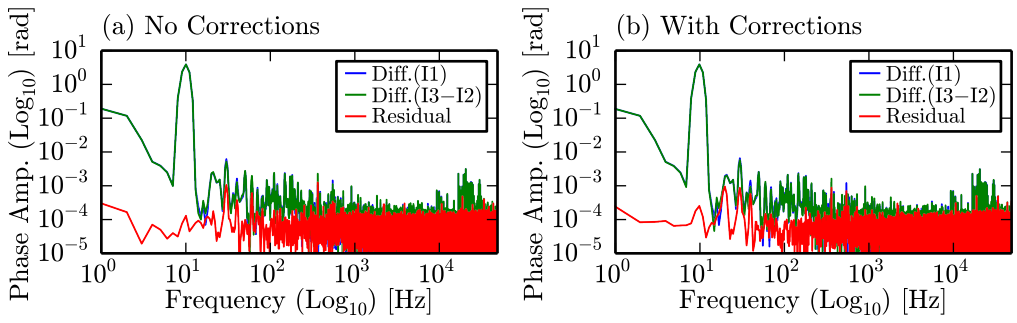

Fig. 10. The Fourier spectra (over 1 s) of the direct and indirect versions of the differential signal from PZT A as well as their residual signal are shown on a double logarithmic scale up to a bandwidth of 48 kHz, without (a) and with (b) corrections according to Sec. 3.2.

#226258 - $15.00 USD Received 4 Nov 2014; revised 4 Mar 2015; accepted 7 Mar 2015; published 3 Apr 2015

Finally Fig. 10 shows the Fourier spectra of the differential phase signals, induced by PZT A and also plotted in the time domain in Fig. 9(c). Figure 10(a) shows the case without any corrections according to Sec. 3.2, while Fig. 10(b) shows the case incorporating these corrections. The spectra of the direct and indirect differential signals in both plots appear virtually indistinguishable and no discernible crosstalk from PZT C at 180 Hz is visible. In both Figs. 10(a) and 10(b), the spectra of the residual signal are free from most noise frequency components that are present in the differential signals, exhibiting a mostly flat noise floor of around $\approx 10^{-4}$ rad, which for the recording time of the Fourier spectra of 1 s corresponds to a noise level of $\approx 10^{-4}\,\mathrm{rad\,Hz^{-0.5}}$. However, in both cases the spectra of the residual signal contains harmonics of the original phase signals at 10 Hz and 180 Hz that can reach levels up to $\approx 10^{-3}$ rad.

4.2. Linearity measurements

Often in prior work on the assessment of cyclic errors in precision interferometry, such as McRae *et al.* [19], a very linear phase change is induced experimentally and the cyclic errors are determined by subtraction of the measured signal from the assumed linear phase change. In the nested MZ setup, the possibility to measure signals in two independent ways allows for a different method to assess the linearity of the measurements without relying on any assumptions of linear movement. In this approach, the residual signal, discussed previously in Sec. 4.1, with its mean removed, is averaged over time and plotted on a two dimensional map as a function of the phases of PZT A (taken from I1) and PZT C (taken from I2). As can be seen in the setup in Fig. 5, the signal from PZT C provides the offset phase to the inner, differential interferometer excited by PZT A and thus all possible phase combinations that can occur in the nested MZ interferometer are covered if both PZT A and C have peak-to-peak phase excitations $> 2\pi$. The maximum absolute residual values occurring in these maps yields an upper bound on the cyclic errors occurring in the combined system of the three constituent interferometers, however, this method cannot determine the cyclic errors of the individual interferometers. This method also assumes that the previously discussed slow polarization drifts can be neglected, which is considered acceptable as the measurements are taken in quick succession. For the purpose of this work, this method allows to qualitatively assess cyclic errors as a function of the window width parameter, σ, and to compare the cases where the corrections according to Sec. 3.2 have or have not been applied.

The results of these measurements are shown in Fig. 11, where the residual measurements described above, recorded over 25 s, are binned and averaged into 20x20 phase sectors. Figures 11(a) and 11(b) show these maps for $\sigma = 0.0075$ and $\sigma = 0.0225$, respectively, in each case both with and without corrections. The residuals in Fig. 11(a) for $\sigma = 0.0075$ are shown as an example for the occurrence of strong cyclic errors, with maximum residual absolute values up to 0.38 rad. In contrast, Fig. 11(b) shows the maps corresponding to the optimal choice of σ at approximately 0.0225. Here the maximum residual absolute values are 3.1 mrad and 4.4 mrad for the cases with and without corrections, respectively, and the maps exhibit a complex pattern that cannot be straightforwardly interpreted. Finally, Fig. 11(c) compares the maximum residual absolute values obtained in this way over a wide range of the window width parameter σ. It can be seen that the best choice of σ for the present configuration is approximately $\sigma = 0.0225$ for both corrected and non-corrected data. Both data sets show a strong increase in non-linear behavior for $\sigma < 0.015$, which can be explained by the strong widening of the baseband crosstalk suppression peaks in Fig. 3 for very small σ. For the case with corrections, a remarkably flat behavior of the maximum residual absolute values exists up to $\sigma = 0.06$, confirming the quality of the applied corrections. Above $\sigma = 0.06$ the cyclic error amplitudes rise in both cases due to the increase in baseline power also evident in Fig. 3. Nevertheless, for $\sigma = 0.0225$ it can

#226258 - $15.00 USD Received 4 Nov 2014; revised 4 Mar 2015; accepted 7 Mar 2015; published 3 Apr 2015

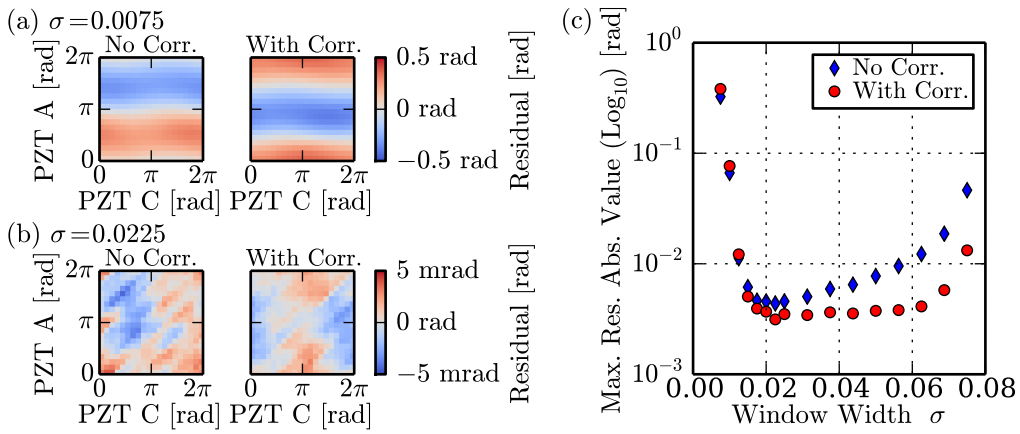

Fig. 11. Residual maps for the cases of (a) $\sigma = 0.0075$ and (b) $\sigma = 0.0225$, note the different colorbar scaling, are shown both with and without corrections according to Sec. 3.2. (c) plots the maximum residual absolute values over a wide range of width parameters σ.

be seen that even in the case without any corrections very linear measurements with maximum cyclic errors of ± 4.4 mrad, dropping to ± 3.1 mrad with corrections applied, can be performed.

4.3. Detuning tolerance

In the final experiment the robustness of the obtainable linearity is tested against detuning of the demodulation parameters. Here the demodulation phase carrier amplitude, A_d, and the signal processing delay, t_sp, were detuned, for all three constituent interferometers simultaneously, from their optimal positions and the resulting maximum residual absolute values were determined using the same method previously employed in Sec. 4.2. For each interferometer, A_d was altered by values of $[-2, 0, 2]$ rad and the t_sp was altered by values of $[-10, 0, 10]$ ns, resulting in nine detuning parameter combinations (a,...,i) that are illustrated in the inset of Fig. 12(a). The window width parameter $\sigma = 0.0225$ was kept constant throughout. As this experiment was performed on a separate occasion from the previous experiments the signal processing delay t_sp had changed by 2 ns compared to Fig. 7(a). This is a typical example of instrumental drift observed

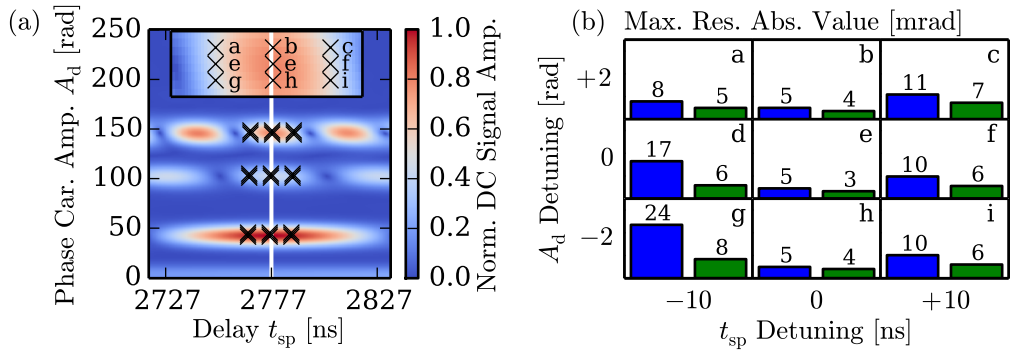

Fig. 12. The positions of the 9 parameter combinations (a,...,i) used are shown on the demodulation parameter map in (a), drawn analogously to Fig. 7(a). The resultant maximum residual absolute values are compared in (b), where uncorrected and corrected results are represented by the blue and green bars, respectively, with values in units of mrad also given.

#226258 - $15.00 USD Received 4 Nov 2014; revised 4 Mar 2015; accepted 7 Mar 2015; published 3 Apr 2015

in t_{sp} and is significantly smaller than the chosen maximum variation of t_{sp} of ± 10 ns used for this experiment. Also no significant drifts of the phase carrier amplitude were ever observed in practice, thus this experiment can be considered a worst-case scenario. The resulting maximum residual absolute values are shown in Fig. 12(b) for the nine detuning parameter combinations used. It is evident that the corrected signal is generally more robust against detuning of the signal processing parameters than the measurements without corrections. Nevertheless, while there is a significant increase in cyclic error amplitude, up to 24 mrad in parameter combination g, there is never a complete breakdown of linearity and the scheme can thus be considered reasonably robust against detuning, especially when the discussed corrections are applied.

4.4. Further discussion

In this work, the optical frequency modulation waveform was deliberately kept simple, using only a pure sinusoidal laser injection current modulation and applying any corrections in post processing only. Another approach that could be explored would be to correct the deviations due to the non-linear injection current to optical frequency modulation characteristic described in Sec. 3.2 by applying a pre-shaped waveform to result in a purely sinusoidal optical frequency modulation. However, intensity modulation associated with laser injection current modulation cannot be corrected in this way and would still require post processing corrections as described. It is thought that the remaining cyclic errors in the residual signal found in Sec. 4.2 originate from non-ideal baseband crosstalk signal suppression leading to crosstalk between constituent interferometers. Issues that were preliminary identified to influence baseband crosstalk suppression were quantization errors due to the limited ADC resolution of 14 bits and photo diode non-linearities causing intermodulation effects. Both these effects need to be investigated in a separate, more in-depth analysis to see whether the observed cyclic errors levels can be minimized further. Nevertheless, highly linear phase measurements exhibiting cyclic errors of 3.1 mrad (0.18°) with the corrections described in Sec. 3.2 applied and 4.4 mrad (0.25°) without any corrections have been demonstrated using this simple scheme and components totaling less than $5k. It is interesting to note that, while not strictly comparable, typical cyclic error amplitudes in precision free-space heterodyne interferometry [19], using sophisticated polarization isolation equipment to achieve high linearity, range from 0.8° to 0.05°, and are thus on the same order of magnitude. Initial observations of the measured noise levels in the phase signals show that these are proportional to the OPD, indicating that noise performance is likely to be dominated by laser phase noise and not by OPD-independent noise sources such as shot, intensity or electronic noise. However, it is also recognized that the application of a window function reduces the effective sampling time while maintaining the noise bandwidth of the measurement chain, which would increase the detrimental effect of shot, intensity or electronic noise. This is further complicated by the possibility of aliased high-frequency noise [20] affecting the quadrature phase signals and therefore this complex noise behavior warrants a thorough future investigation. As discussed in Sec. 2.4, the spatial resolution of this scheme is directly proportional to the optical frequency modulation amplitude used, with no other fundamental limits. Thus, if the diode laser used in this work was replaced with, for example, a widely tunable micro-electromechanical system based external cavity laser (MEMS-ECL), such as the one used by Baumann *et al.* [21], with its sinusoidal frequency modulation amplitude of $\Delta f = 1$ THz at 1 kHz modulation frequency, an increase in spatial resolution of a factor of 56 should be achievable. Therefore, in such a system, constituent interferometers differing by physical path differences < 3 mm could be resolved and interrogated with full interferometric phase resolution.

#226258 - $15.00 USD Received 4 Nov 2014; revised 4 Mar 2015; accepted 7 Mar 2015; published 3 Apr 2015

5. Conclusion

In this work, a novel range-resolved interferometric signal processing technique has been presented that uses sinusoidal modulation of the optical frequency of a laser diode. Using an appropriate time-variant carrier and a smooth window function to suppress contributions from undesired signal components in the demodulation process, highly linear phase signals can be obtained. Due to the proportionality of the phase carrier amplitude to the OPD in optical frequency modulation, multiple constituent interferometers can be multiplexed. The OPDs of the constituent interferometers are continuously and independently variable, subject to a minimum OPD separation. Using the multiplexing and self-referencing properties of this scheme, novel interferometric configurations, such as the nested MZ interferometer, can be realized. In this implementation cyclic errors as low as 0.18° were realized at a spatial resolution of 15 cm in fiber for multiplexing three constituent interferometers with a measurement bandwidth of 48 kHz. It has been shown that non-ideal effects that arise due to injection current modulation of a laser diode, such as intensity modulation and deviations from the ideal sinusoidal optical frequency modulation, can easily be compensated in post processing. However, even without these corrections, highly linear (cyclic errors $< 0.26^\circ$) measurement results can still be obtained. It was further shown that the technique is reasonable robust against detuning by instrumental drift.

Acknowledgments

The authors acknowledge the support of the Engineering and Physical Sciences Research Council (EPSRC) UK, via grant EP/H02252X/1 and EP/G033900/1. (For inquiries relating to access to the research data or other materials referred to in this article, please contact Cranfield University Library and Information Services: `library@cranfield.ac.uk`).

#226258 - $15.00 USD Received 4 Nov 2014; revised 4 Mar 2015; accepted 7 Mar 2015; published 3 Apr 2015

2015-04-03

Range-resolved interferometric signal processing using sinusoidal optical frequency modulation

Kissinger, Thomas

Optical Society of America (OSA)

Kissinger T, Charrett TOH, Tatam RP. (2015) Range-resolved interferometric signal processing using sinusoidal optical frequency modulation. Optics Express, Volume 23, Issue 7, pp. 9415-9431
http://dx.doi.org/10.1364/OE.23.009415